This is the authors' version of the article published in Smart Materials and Structures. Changes were made to this version by the publisher prior to publication. The final version is available at https://doi.org/10.1088/1361-665X/ac3ebd

Resistive Heating of a Shape Memory Composite: Analytical, Numerical and Experimental Study

Clara Pereira Sánchez[1], Maxime Houbben[2], Jean-François Fagnard[1], Philippe Laurent[1], Christine Jérôme[2], Ludovic Noels[3] and Philippe Vanderbemden[1]

[1] Department of Electrical Engineering and Computer Science, University of Liège, Liège, Belgium
[2] CERM, CESAM-RU, University of Liège, Liège, Belgium
[3] Department of Aerospace and Mechanical Engineering, University of Liège, Liège, Belgium
E-mail: capereira@uliege.be

Abstract

This work investigates in detail the Joule resistive heating phenomenon of electroactive Shape Memory Composites (SMC) when an electric current is injected at constant power. The SMC is a covalent poly(ε-caprolactone) network filled with 3 wt% of multiwall carbon nanotubes. The resistive heating of the SMC is studied by means of surface temperature measurements, analytical formulas and a coupled 3D thermo-electric numerical model. Analytical expressions are derived for the 2D temperature distribution within a parallelepipedic SMC, either with constant or linearly-dependent electrical resistivity. These analytical expressions can be used to investigate the influence of geometrical and material parameters in the steady-state temperature and its distribution across the sample. The results also allow one to identify the parameters that are crucial for predicting the temperature rise due to resistive heating: the temperature dependence of the resistivity has little effect on the steady-state temperature, whereas the thermal conductivity plays a significant role. The time-dependent temperature is shown to be related to the particular temperature dependence of heat capacity. Furthermore, the presence of external objects (clamps or grips) used during the shape memory cycle must be taken into consideration for a certain temperature to be reached since they result in a lower steady-state temperature and a slower resistive heating phenomenon. With the findings presented in this work, accurate resistive heating can be predicted for a SMC upon the injection of an electric current at constant power.

Keywords: shape-memory, composites, carbon nanotubes, resistive heating, electroactivation

1. Introduction

Shape memory polymers (SMP) and their composites (SMC) are smart materials having morphing capabilities that can be applied in aerospace, biomedical or textile engineering [1]. Concerning thermo-responsive SMP, the shape memory cycle is achieved by deforming the material from its permanent to its temporary shape once heated above its transition temperature [2]. After the deformation has taken place, the temporary shape can be fixed by cooling down the material below the transition temperature. Re-heating the material again past its transition temperature will lead to the shape recovery, i.e. return to its permanent shape. Conventionally, the shape change is triggered with direct heating by placing the material close to a heat source. This technique, relying on an external heater, is sometimes impossible, problematic or even hazardous. In the recent years, effort has been put into generating the shape recovery remotely [3] by using an electric current [4][5], a magnetic field [6][7], light [8][9], or pH [10],[11].

SMC controlled and triggered by electric currents have gained more and more interest within the range of shape memory materials. This is due to the rapid and efficient process that is the Joule resistive heating, since the heat is generated directly within the material itself. For the Joule effect to take place, however, the SMP needs to be electrically conductive enough. That is the reason why conductive fillers are introduced into the SMP matrix. The amount of conductive

fillers required to reach the percolation threshold, i.e. for having an electrically conductive network within the SMC, depends on several factors such as the nature of the fillers themselves, their size and shape, etc [12]. Some examples of electrically conductive fillers include graphene [13], carbon nanotubes [14][15], carbon (nano)fibers [4][16], carbon black [5][12], and metal nanoparticles [17]. An added value of utilizing these fillers is, in most cases, the improved mechanical properties of the resulting composite [18][19].

In an electroactivation process, the amount of heat generated within the material depends on the electrical current being injected I, on the geometry of the SMC and its electrical resistivity ρ_e. In order to generate a well-defined shape change, it is necessary to be able to accurately predict the temperature increase resulting from the heat generated within the material. The temperature increase depends on the parameters cited above and on those related to the heat transfer process, both within the SMC (thermal conductivity κ, heat capacity C_p and density ρ_m) and at the interface between the SMC and its environment.

An additional characteristic of this problem is that the temperature is time-dependent and non-uniform within the material. This affects directly the amount of heat generated since ρ_e is, in general, found to be dependent on the local temperature T of the SMC $\rho_e(T)$ [20][21]. Although much experimental effort was devoted to achieve a significant, fast and uniform temperature increase by electroactivation in SMC samples [4], there is however little analysis on how the geometric and physical parameters affect the temperature dependence of the temperature distribution, in particular when the electrical resistivity is time-dependent (through its dependence on temperature). Due to the nature of the SMC, the material structure changes during heating (specially after the transition temperature), which affects the material properties in a non-monotonic way and may influence the resistive heating behavior of these materials.

The objective of the present work is to investigate in detail the mechanism of resistive heating in SMC subjected to an electric current. Whenever possible, analytical expressions for the temperature evolution in the samples will be determined. The present study will address the following issues:

(i) to predict the temperature that would be reached upon the injection of a given electrical current I,

(ii) to identify the parameters that are crucial for predicting the temperature and to understand how any variation of them affects the final outcome.

In this work the SMC sample is assumed to have a parallelepiped shape and is subjected to resistive heating by an electric current injected in parallel to its longer dimension, as schematically illustrated in Figure 1(a). This geometry where one considers the sample alone is referred to as the "bare SMC" geometry: the thermal characteristics of the electrical contacts are neglected and the heat losses through the lead wires are assumed to be zero. In this configuration three cases will be studied and compared:(i) the analytical predictions using models of increasing complexity, (ii) numerical results obtained using Finite Element Method (FEM) with the commercial software Ansys, and (iii) experimental results of resistive heating.

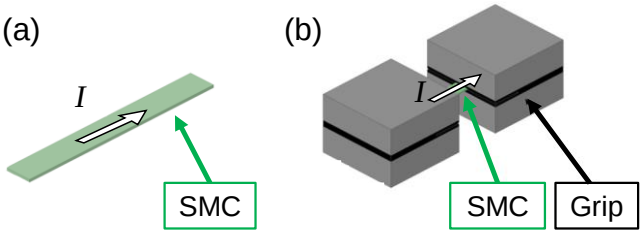

Figure 1: (a) Sketch of "bare SMC" geometry. (b) Sketch of "SMC with grips".

Lastly, the main changes brought by using structures of much larger size in contact with the SMC will be considered. For instance, when studying the shape memory properties of a SMC, one needs to deform the SMC and/or measure the shape recovery force. In practice, this is achieved using grips or clamps, whose thermal and electrical properties may significantly affect the resistive heating of the SMC sample under investigation. This would lead to a different final temperature and thermal time constant. In this work, the difference in resistive heating of the SMC will be studied when left by itself or when mounted in realistic conditions using both the FEM analysis and experiments. The geometry investigated will involve two grips of dimensions that are much larger than the sample, as schematically illustrated in Figure 1(b). This geometry will be referred to as "SMC with grips".

The experimental work will focus on a SMC formed by chemically cross-linked poly(ε-caprolactone) (PCL) filled with 3 wt% of multiwall carbon nanotubes (MWCNT). MWCNT are electrically conductive fillers that have superior electrical and thermal properties while having low density and high aspect ratio. This last property facilitates the creation of the conductive network inside of the composite, or, similarly, the percolation threshold can be obtained with a smaller loading of conductive filler, thus having less impact in the mechanical properties. Preliminary experiments showed that the average resistivity of SMC with >1 wt% of CNT is below 80 Ωm, i.e. low enough to enable current driven heating. In the present study, the concentration of fillers was chosen to be 3 wt% for two reasons: (i) compared to lower CNT content, the reproducibility of resistive heating and shape-memory cycle of SMC with 3 wt% CNT is much better, (ii) to ensure enough electrical conductivity of the SMC after the potential deformation during the shape memory cycles. The reason is that deformation will cause the CNT to be placed further apart and the conductivity to drop considerably. By choosing 3 wt%

of CNT, the amount of elongation for which the SMC can be used for shape memory is higher than for lower contents.

2. Analytical study

The analytical study of the resistive heating is carried out for the "bare SMC" geometry illustrated in Figure 1(a). In this study, it is always assumed that the SMC sample is heated at a constant power P_0 switched on at $t = 0$, as illustrated schematically in Figure 2(a). If the electrical resistance of the SMC sample is assumed to be constant, this corresponds to a constant current $I = I_0$. Otherwise the current $I(t)$ is adjusted continuously by the power supply during the resistive heating process to maintain the total electric power constant for $t > 0$.

The SMC sample is always placed at a starting temperature $T(t = 0) = T_0$. During heating up, the focus will be on both the time-dependent heating $T(t) - T_0$ (transient study) and the temperature increase reached at $t \to \infty$, i.e. $T_s - T_0$ (steady-state).

Three different analytical cases with increasing complexity will be analysed, as illustrated in Figure 2(c): (1) uniform T, (2) non-uniform $T(x, y)$ and temperature-independent ρ_e and, (3) non-uniform $T(x, y)$ and linearly temperature-dependent ρ_e. The geometry considered is that of Figure 2(b) with length L, width $2a$ and thickness $2b$; one assumes L>>a and L>>b. For the $T(x, y)$ determination in the 2D analytical model, one assumes an infinite length L.

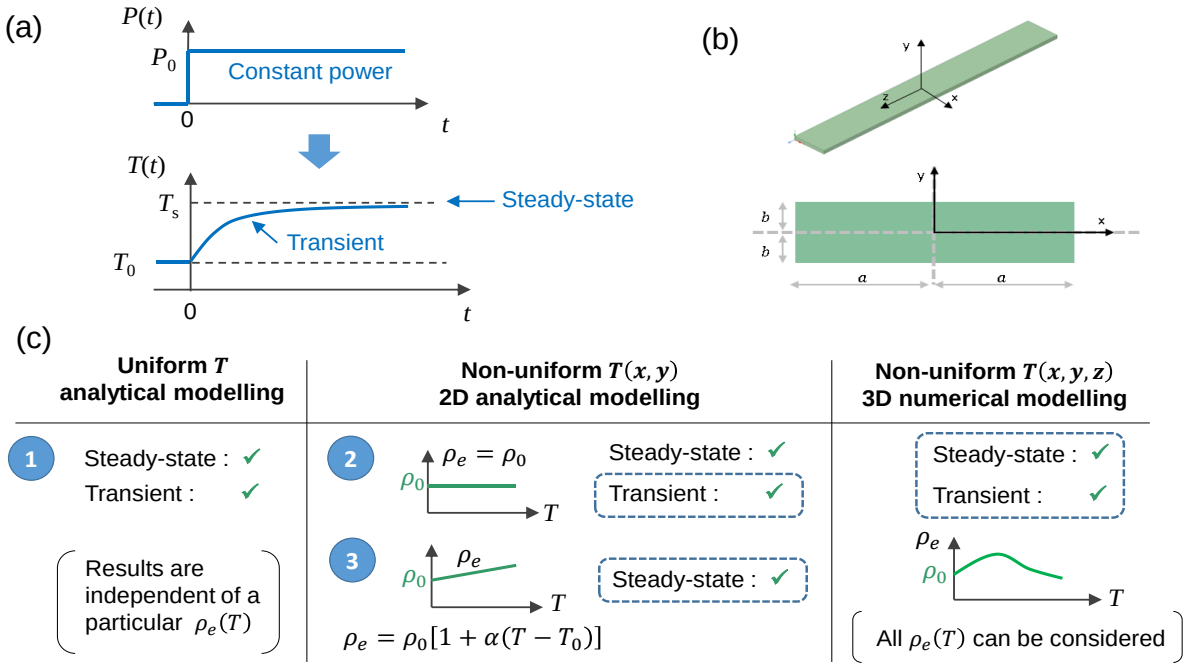

Figure 2: (a) Sketch of power step applied to the sample and resulting temperature evolution with time. (b) Schematic illustration of the "bare SMC" geometry of the Shape Memory Composite parallelepiped samples considered in the investigation of resistive heating. (c) Summary of the cases investigated either analytically (this section) or numerically (section 3). The blue dashed frames refer to cases that were not described previously in the literature and that are investigated in the framework of this paper.

For all for cases, the heat exchange between the SMC and air happens only due to convection: for the experimental conditions in this work, conduction of heat through air and radiation heat transfer can be neglected since the Nusselt number (Nu) is well above unity and the radiation equivalent Nusselt number (Nu_r) is much smaller than one (see appendix I for Nu and Nu_r). Convection heat transfer from the surfaces of the samples to the ambient is assumed to be as described by Newton's law of cooling. The convection coefficient h of all six faces is assumed to be the same. The effective area A_T is assumed to be constant, i.e. negligible thermal expansion. The material is assumed homogeneous, isotropic and, except for ρ_e as described per each case, its properties are assumed to be temperature-independent. The temperature dependence of the resistivity $\rho_e(T)$ is taken into consideration because it directly affects local power dissipated during resistive heating.

2.1 Uniform T

This is the simplest and the most straightforward model [22] for which the solution is recalled below. This assumption of uniform T corresponds to relatively high thermal conductivity meaning that the Biot number $Bi = ha/\kappa$ tends to zero. The ordinary differential equation that governs the heat transfer is given in equation 1, where m is the mass of the sample, C_p is the heat capacity, A_T is the addition of the six surfaces of the parallelepiped ($A_T = 4La + 4Lb + 8ab$) and P_0 is the power generated by Joule effect.

$$mC_p\frac{dT}{dt} = -hA_T(T(t) - T_0) + P_0 \quad (1)$$

Since the current is injected at constant power P_0, any possible temperature dependence of the resistivity ρ_e does not affect the results because $P_0 = (\rho_e\, LI^2)/(4ab)$ is kept constant. Under these assumptions, the resistive heating is given in equation 2, where τ is the time constant (equation 3) and the steady-state temperature difference is $T_s - T_0$ (equation 4).

$$T(t) = T_0 + (T_s - T_0)\left(1 - \exp\left(-\frac{t}{\tau_0}\right)\right) \quad (2)$$

$$\tau_0 = \frac{mC_p}{hA_T} \quad (3)$$

$$T_s - T_0 = \frac{P_0}{hA_T} \quad (4)$$

2.2 Non-uniform T, temperature-independent ρ_e.

When T is not assumed to be uniform, it is necessary to consider the finite value of the thermal conductivity κ. The 2D heat balance equation is that of equation 5, where T is the temperature at any point of the slice (x, y) at any given time t and ρ_m is the density of the material. The local power per unit volume $q_0 = P_0/V$ is both time and temperature-independent. Convective boundary conditions are assumed along the 4 faces of the sample $x = \pm a$ and $y = \pm b$.

$$\frac{\partial^2 T(x,y,t)}{\partial x^2} + \frac{\partial^2 T(x,y,t)}{\partial y^2} + \frac{q_0}{\kappa} = \frac{\rho_m C_p}{\kappa}\frac{\partial T(x,y,t)}{\partial t} \quad (5)$$

The total temperature $T(x,y,t)$ is the addition of the steady-state temperature $T_s(x,y)$ plus a transient part $T_t(x,y,t)$. The steady-state part of the problem $T_s(x,y)$ was solved by Carslaw and Jaeger [23], chapter 5.5, and is shown in equations 6 and 7. The step-by-step solution of the transient part $T_t(x,y,t)$ can be found in appendix II. It is given in equations 8 to 11.

$$T_s(x,y) = T_0 + \frac{aq_0}{h}\left(1 + \frac{\mathrm{Bi}}{2}\left(1 - \left(\frac{x}{a}\right)^2\right)\right) - \frac{4q_0 a}{h}\sum_{n=1}^{\infty}\frac{\mathrm{Bi}\sin(\Lambda_n)\cos\left(\Lambda_n\frac{x}{a}\right)\cosh\left(\Lambda_n\frac{y}{a}\right)}{\Lambda_n^2[2\Lambda_n + \sin(2\Lambda_n)]\left[\frac{\Lambda_n}{\mathrm{Bi}}\sinh\left(\Lambda_n\frac{b}{a}\right) + \cosh\left(\Lambda_n\frac{b}{a}\right)\right]} \quad (6)$$

where

$$\Lambda_n\tan(\Lambda_n) = \frac{ha}{\kappa} = \mathrm{Bi} \quad (7)$$

$$T_t(x,y,t) = \sum_{n=1}^{\infty}\sum_{m=1}^{\infty} C_{3,nl}\cos\left(\Lambda_n\frac{x}{a}\right)\cos\left(\mathrm{H}_l\frac{y}{b}\right) * \exp\left(-\frac{\kappa}{\rho_m C_p}\left(\frac{\Lambda_n^2}{a^2} + \frac{\mathrm{H}_l^2}{b^2}\right)t\right) \quad (8)$$

$$\mathrm{C}_{2,\mathrm{nl}} = -\frac{4a^2 bq_0\sin(\mathrm{H}_l)[(\Lambda_n^2 + \mathrm{Bi})\sin(\Lambda_n) - \Lambda_n\mathrm{Bi}\cos(\Lambda_n)]}{h\Lambda_n^3\mathrm{H}_l} + 4q_0 a^3\mathrm{Bi}\sin(\Lambda_n) * \frac{\left(\Lambda_n\sinh\left(\Lambda_n\frac{b}{a}\right)\cosh(\mathrm{H}_l) + \frac{a}{b}\mathrm{H}_l\cosh\left(\Lambda_n\frac{b}{a}\right)\sin(\mathrm{H}_l)\right)}{h\Lambda_n^3\left[\frac{\Lambda_n}{\mathrm{Bi}}\sinh\left(\Lambda_n\frac{b}{a}\right) + \cosh\left(\Lambda_n\frac{b}{a}\right)\right]\left[\Lambda_n^2 + \mathrm{H}_l^2\left(\frac{a}{b}\right)^2\right]} \quad (9)$$

$$C_{3,nl} = \frac{4\Lambda_n\mathrm{H}_l\, C_{2,nl}}{ab[2\Lambda_n + \sin(2\Lambda_n)][2\mathrm{H}_l + \sin(2\mathrm{H}_l)]} \quad (10)$$

$$\mathrm{H}_l\tan(\mathrm{H}_l) = \mathrm{Bi}\frac{b}{a} \quad (11)$$

In the particular case $\mathrm{Bi} = 0$ (uniform temperature), it can be shown that the above equations reduce to equations 2 to 4 except that the steady-state temperature increase $P_0/(hA_T) = (q_0\, V)/(hA_T)$ appearing in equations 2 to 4 is now replaced by $(q_0 ab)/(h(a+b))$. This difference is due to the 2D approximation assuming an infinite length L. The ratio of the volume over the lateral surface V/A_T is equal to $(4Lab)/(4La + 4Lb + 8ab)$, reducing to $ab/(a+b)$ when L is infinite. In practice, however, SMC samples have a large but finite L. In order to be able to compare the 2D analytical modelling developed in this section to 3D modelling and experiment, a geometric correction factor (GCF) is to be multiplied by the local dissipated power q_0.

$$\mathrm{GCF} = \frac{L(a+b)}{La + Lb + 2ab} \quad (12)$$

A frequent situation is the one for which Bi << 1. In this case, equations 6 and 7 can be approximated using Taylor series expressions for the trigonometric and hyperbolic functions (see appendix III). One obtains equation 13, which predicts perfectly elliptic isothermal lines. Moreover, it shows that the temperature profile that can be obtained using a surface temperature measurement (along the plane y = b) is, in first approximation, parabolic across the width of the slab.

$$T_s(x,y) \approx T_0 + \frac{q_0}{h}\left(\frac{ab}{a+b}\right) + \frac{q_0}{\kappa}\left\{\frac{ab(a^2 + 6ab + b^2)}{6(a+b)^2} - \frac{ab}{2(a+b)}\left[a\left(\frac{x}{a}\right)^2 + b\left(\frac{y}{b}\right)^2\right]\right\} \quad (13)$$

In particular, the temperature difference between the center $(0, \mathrm{b})$ and the edge (a, b) is given by

$$T_s(0,b) - T_s(a,b) \approx \frac{q_0 ab}{2\kappa}\left(\frac{a}{a+b}\right) \quad (14)$$

The average temperature over the top surface of the sample y = b) is given by

$$\langle T_s(x,b)\rangle \approx T_0 + \frac{q_0}{h}\left(\frac{ab}{a+b}\right) + \frac{2q_0 ab^2(a-b)}{3\kappa(a+b)^2} \quad (15)$$

Equation 13 can also be used to predict approximately the maximum temperature difference within the slab cross-section, $T_s\,(0,0) - T_s\,(a,b) \approx (q_0 ab)/(2\kappa)$.

2.3 Non-uniform T, temperature-dependent ρ_e

A temperature-dependent resistivity $\rho_e(T)$ is considered here. If one assumes a linear dependence $\rho_e(T) = \rho_0[1 + \alpha(T - T_0)]$, the transient heat transfer governing equation in 2D cannot be solved analytically (for numerical results refer to section 5.3). Therefore, for this case, only the steady-state temperature is considered and solved.

Because ρ_e depends on $T(x,y)$, then it is also non-uniform $\rho_e(x,y)$. This means that even for a current injected at constant power P_0, the local dissipated power $q(x,y)$ will not follow exactly the expression for $\rho_e(x,y)$ because the current will re-distribute in order to flow preferably through the path of least resistance. If one assumes that the local resistive heating is kept moderate such that $|\alpha(T(x,y) - T_0)| \ll 1$, $q(x,y)$ is that of equation 16, where $\langle T \rangle$ denotes the average temperature over the sample cross-section. The proof of this equation is given in appendix IV.

$$q(x,y) \approx q_0 \{1 - \alpha[T(x,y) - \langle T \rangle]\} \quad (16)$$

Since $\langle T \rangle$ is not known, one can assume it is given by $\langle T \rangle = T_0 + \tilde{T}$ where $\tilde{T}$ denotes the average steady-state resistive heating when $\alpha = 0$, i.e. $\langle T \rangle$ is the average of equation 6. The local dissipated power $q(x,y)$ can then be inserted into the steady-state heat balance given by equation 17.

$$\frac{\partial^2 T(x,y)}{\partial x^2} + \frac{\partial^2 T(x,y)}{\partial y^2} + \frac{q(x,y)}{\kappa} = 0 \quad (17)$$

The solution to the non-homogeneous partial differential equation with the same boundary conditions as those specified in section 2.2 is given in equation 18. The necessary coefficients are given below in equations 19 to 22. The step-by-step solution is given in appendix V.

$$T(x,y) = \langle T \rangle + \sum_{n=1}^{\infty} C_{6,n} \cos\left(\Lambda_n \frac{x}{a}\right) \cosh\left(C_{7,n} \frac{y}{a}\right) + \frac{1}{\alpha} + C_4 \cosh\left(C_5 \frac{x}{a}\right) \quad (18)$$

$$C_4 = \frac{-\frac{1}{\alpha} - \tilde{T}}{\frac{C_5}{\mathrm{Bi}} \sinh(C_5) + \cosh(C_5)} \quad (19)$$

$$C_5 = \sqrt{\frac{q_0}{\kappa} \alpha a^2} \quad (20)$$

$$C_{6,n} = \frac{-4\left(\frac{1}{\alpha} + \tilde{T}\right) C_5^2 \sin(\Lambda_n)}{(C_5^2 + \Lambda_n^2)[2\Lambda_n + \sin(2\Lambda_n)]\left[\frac{C_{7,n}}{\mathrm{Bi}} \sinh\left(C_7 \frac{b}{a}\right) + \cosh\left(C_{7,n} \frac{b}{a}\right)\right]} \quad (21)$$

$$C_{7,n} = \sqrt{\frac{q_0}{\kappa} \alpha a^2 + \Lambda_n^2} \quad (22)$$

In the particular case $\alpha = 0$ (temperature-independent resistivity), it can be checked that the above equations reduce to equation 6, as expected intuitively.

3. Numerical modelling

The numerical study on the resistive heating of the SMC samples is carried out using the commercial finite element method (FEM) software Ansys. A thermal-electric module is added in Ansys Workbench and appropriately modified by inserting APDL (Ansys Parametric Design Language) commands in order to render it transient. APDL commands are also used to specify the time step, and to enforce the same type of quadratic element throughout the SMC geometry. The homogenized thermal and electrical material properties of the SMC are obtained from experimental measurements on the SMC samples (see section 5.1 and 5.2) and are assumed to be homogeneous. The thermal expansion of the SMC is assumed to be negligible. As for the analytical study, conduction and radiation heat transfer to surroundings are neglected.

The two geometries illustrated in Figure 1 are considered. For the "bare SMC" geometry shown in Figure 1(a), it is assumed that the heat transfer through the wire leads used for injecting the electric current is negligible.

Convection heat transfer boundary conditions are used in all six faces of the parallelepiped. Similar to the experimental conditions and to the analytical study, the current injected is adjusted continuously during the resistive heating process to maintain the total injected electric power constant, even when a temperature-dependent resistivity is considered. Using numerical modelling, it is possible to consider any temperature dependence of the material properties, including electrical resistivity or heat capacity.

Convergence is specified on the voltage and temperature calculations, both with a tolerance value of $5 \cdot 10^{-3}$ with the Euclidean norm. Newton-Raphson linearization method is chosen to cope with the nonlinearities of some material properties with a distributed sparse matrix direct solver. The mesh is built with quadratic elements SOLID226 and SURF152. For all information concerning the chosen formulation, solver type, or elements, one can refer to the Ansys Mechanical User's Guide [24].

The FEM model is also run in the "SMC with grips" geometry as shown in Figure 3. These grips are made of aluminum and covered with a rubber layer in order to electrically insulate them from the SMC sample. The size and material properties of the rubber and aluminum of the grips are taken from the literature or from the manufacturer whenever possible. All used geometrical and material parameters are summarized in Table 1. The contact between the different materials of the geometry is set as Bonded with elements CONTA174 and acts as a pure thermal contact since no mechanical loads are present. The interface thermal conductance at the contact between the SMC and the grips

(1000 $W \cdot m^{-2} \cdot K^{-1}$) and the convection coefficient of the grips (30 $W \cdot m^{-2} \cdot K^{-1}$) are estimated to best fit the experimental results of resistive heating. The time-step is set as automatic in Ansys with an initial time-step of 10^{-5} s and a maximum time-step of 10^{-1} s.

The symmetry of both geometries was considered in order to reduce the computational time. With that in mind, a mesh convergence study was performed for each geometry in order to determine the minimum number of elements required to give a prediction of resistive heating that is independent of the mesh size. The convergence study can be seen in appendix VI. For the "bare SMC" and the "SMC with grips" the number of elements used are 2500 and 18500 respectively.

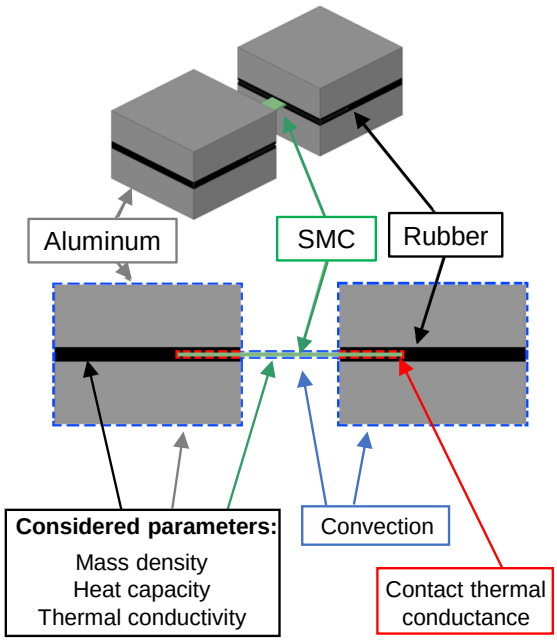

Figure 3: Sketch of "SMC with grips" geometry showing the Shape Memory Composite sample, rubber and aluminum grips used for modelling, considered material parameters and boundary conditions.

Table 1: Geometrical and material properties for the aluminum and rubber grips used in the Ansys numerical simulation for "SMC with grips" geometry

	Aluminum	Rubber
Size [mm^3]	30x30x11	30x30x1
ρ_m [$kg \cdot m^{-3}$]	2689	950
C_p [$J \cdot kg^{-1} \cdot K^{-1}$]	951	1350
κ [$W \cdot m^{-1} \cdot K^{-1}$]	237.5	0.24
ρ_e [$\Omega \cdot m$]	2.8e-8	4.3e8

4. Experiment

4.1 Processing of Shape Memory Composite Samples

The PCL used in this work was obtained by end-groups functionalization of commercially available star-shaped PCL samples (CAPA™ 4801, Perstorp®) according to the procedure reported in [25]. In order to prepare the SMC, stoichiometric amounts in reactive groups (furan and maleimide moieties) of PCL_{76}-4FUR and PCL_{76}-4MAL powders were grinded together in a mortar and then mixed with 3 wt% of MWCNTs (Nanocyl 7000, properties given in appendix VII). This mixture was melt-blended at 105 °C in a 6 cm^3 co-rotating twin screw mini-extruder (Xplore, DSM) for 60 min at 150 rpm. After extrusion, the polymer blend was shaped to a flat sheet of 0.7 mm thick in a hot press under a load of 75 N for 90 seconds at 105°C and then let to cool down to room temperature. A post-curing is applied for 3 days at 65 °C in a ventilated oven under load.

4.2 Measurement of thermal properties

Differential scanning calorimetry (DSC) was performed using a DSC Q500 (TA Instruments) calibrated with indium. Two heating ramps (3 $°C \cdot min^{-1}$) were applied to the sample between −80 and 100 °C. The melting temperature (T_m, the transition temperature of this SMC) and melting enthalpy (ΔH_m) were recorded during the second heating ramp to be 42 °C and 52.48 $J \cdot g^{-1}$ respectively, which corresponds to a crystallinity ratio of 37.6%. The evolution of the C_p of the SMC as function of T was also measured.

Thermal conductivity measurements were performed with a bespoke experimental system whose details are reported in [26]. Disc samples of 13.94 mm diameter are punched out of a 1.86 mm thick SMC plate. The surfaces of the samples are cleaned with isopropanol and coated with silver paste (Agar scientific Electrodag 1415) for better adhesion and thermal contact between the disc and the sample holder. The measurements are carried out at a pressure $<5 \cdot 10^{-8}$ mbar.

4.3 Resistive heating experiments

Rectangular samples are cut from a SMC sheet of 0.7 mm thick. The length and width of the nominal rectangular samples are 25 and 3 mm respectively. The surface of the samples is cleaned with isopropanol. Four electrodes are painted on the surface of the samples with silver paste and thin wire leads are placed on them so that the injected current flows through the length of the sample in a four-point measurement configuration.

A LabVIEW program controls a Keithley 2400 current source and a Keithley 2001 voltmeter, from which the resistivity of the samples ρ_e is calculated. The LabVIEW program controls the devices so that the power is kept constant and equal to 0.1 W. The temperature on the XZ front surface of the sample is measured using an infrared thermal camera (COX CX320) that was previously calibrated in-house.

For the resistive heating experiments on the "bare SMC" samples, the sample is suspended vertically on air with its longest side perpendicular to the horizontal by making use of

the mechanical properties of the lead wires. The temperature measurement region excludes the electrodes in order to avoid errors in due to the difference emissivity of the silver and the SMC itself. For the resistive heating experiments on the "SMC with grips", the grips used in the experiment (AML instruments TH240k vise grip) are made of aluminum with a layer of nitrile rubber covering the surfaces in contact to the SMC. The nitrile rubber serves to electrically insulate the SMC from the grips themselves. The sample is placed vertically between the grips with a quarter of its length trapped at each grip end, i.e. half of its length is left free to measure the temperature on its surface with the infrared thermal camera.

5. Results and discussion

5.1 Material properties of SMC

The measured heat capacity of the SMC as a function of T is shown in Figure 4(a). This temperature dependence is used for the numerical study. For the analytical study a constant value of 2.02 J·kg^{-1}·K^{-1} is used instead, corresponding to the average between 25 and 50 °C.

The κ is measured on three different samples of SMC at three different power levels, i.e. 61, 122 and 244 mW. Each measurement is carried out twice. The average value of κ measured is 0.22 ± 0.02 W·m^{-1}·K^{-1}.

The density of the SMC is measured to be 1200 kg·m^{-3}.

5.2 Experimental results of resistive heating derived parameters

The resistivity of SMC samples during resistive heating is calculated from the measured voltage across them in order to adjust the injected current to maintain a constant power of 0.1 W. At room temperature, the resistivity of the samples is 0.050 ± 0.015 Ω·m. Figure 4(b) shows the relative resistivity when compared to its value at room temperature as a function of the average temperature on the surface of the samples. There are two very distinguishable regions: for $T < T_m$, ρ_e increases with temperature and for $T > T_m$, ρ_e decreases. These two regions have already been reported [21]. For $T < T_m$, the resistivity increases with temperature because the polymer expands and the MWCNT are placed further away from each other. For $T > T_m$ the resistivity decreases with temperature due to the alignment of MWCNT along the path of the current.

The curve of Figure 4(b) is discretized in temperature intervals in which the temperature coefficient α is assumed constant; the average values of the slope α below and above T_m are indicated on the graph.

The overall convection coefficient h is estimated from the measurement of the steady-state temperature T_s after a resistive heating experiment. For this the constant temperature analytical model (equation 4) is used. For the SMC samples, the average h for different resistive heating ranges investigated is estimated to be 25 W·m^{-2}·K^{-1}.

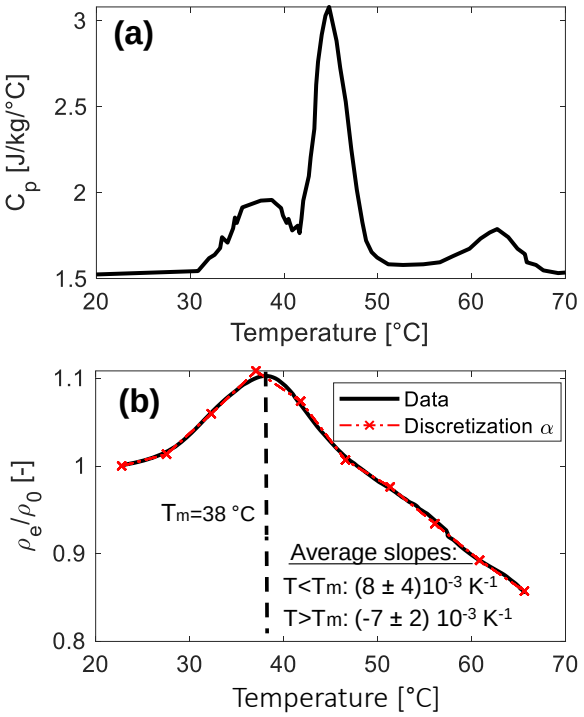

Figure 4: Temperature dependence of (a) the heat capacity and (b) the resistivity of the Shape Memory Composite.

5.3 Resistive heating results on the "bare SMC"

Figure 5(a) shows a sketch of a SMC sample prepared for resistive heating measurements and the experimental steady-state temperature distribution due to resistive heating of an average sample of SMC. The experimental temperature (averaged over the SMC top surface) increases with time as a result of the resistive heating phenomenon for a SMC sample is shown in Figure 5(b) compared to the transient analytical results of section 2.1 and 2.2. It can be first noticed the very satisfactory agreement between the resistive heating experimental data and the simplest model assuming infinite thermal conductivity (uniform T). Since equation 4 from this model was used to find the convection coefficient h, the perfect match with the steady-state temperature is expected. The results plotted in Figure 5(b) show that the whole experimental $T(t)$ curve can be reasonably predicted with the uniform T model as well (dotted line). When a finite thermal conductivity κ is considered, the temperature of the sample is not uniform. The 2D analytical model (equations 6 and 8) run with the experimental data and the geometric correction factor (equation 12) allows one to predict the temperature distribution along the top surface of the sample ($y = b$) and to calculate its average value, plotted in Figure 5 (plain line).

As it can be seen, the 2D analytical approximation predicts a higher steady-state temperature than that of the isothermal model. This can be explained by the internal temperature gradients caused by the finite value of κ. Equation 14, obtained in the approximation Bi << 1, can be used to estimate analytically the difference in the steady-state temperature predicted by the two models; using this procedure one obtains 1.8 ºC. This value reasonably agrees with the difference of 1.1 ºC observed in Figure 5(b), even though the experimental Bi value in the experiment is 0.16.

Additionally, the time dependence of the resistive heating phenomenon is highly dependent on C_p. As Figure 5(b) shows,

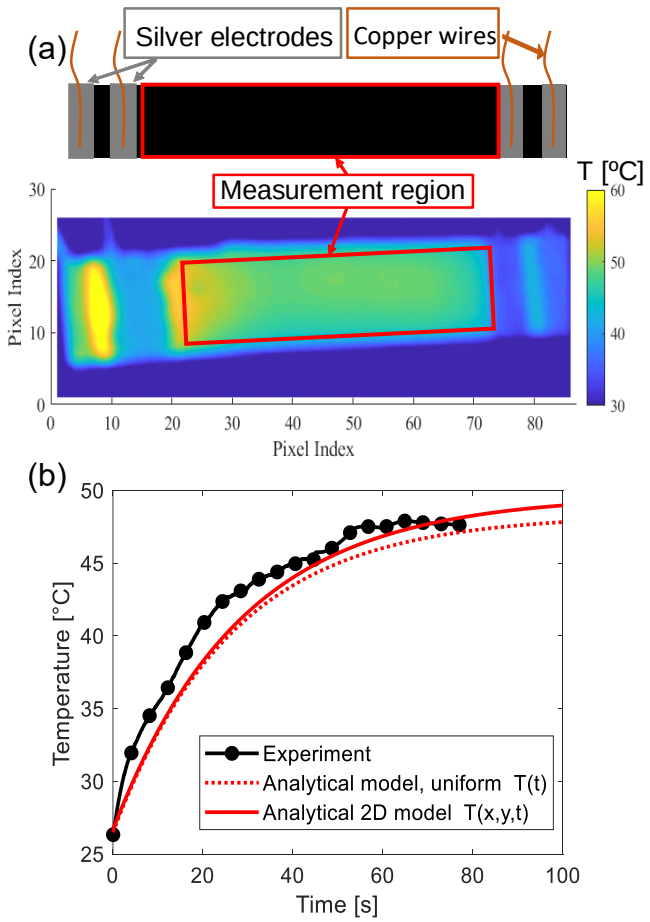

Figure 5: (a) Schematic illustration of a SMC sample with electrodes and wires placed in a four-point configuration and experimental steady-state temperature distribution along the SMC surface ($y = b$). (b) Experimental time dependence of the average temperature over the surface of the SMC sample (black) and calculated analytical temperature (red): uniform T approximation (section 2.1) and non-uniform T and temperature-independent ρ_e evaluated at $y = b$ (section 2.2).

analytical expressions are unable to capture the transient characteristics of resistive heating due, mainly, to a constant C_p. Figure 6 compares the experimental and analytical results to those obtained by the 3D numerical model, run either at constant C_p or using the full $C_p(T)$ temperature dependence observed in Figure 4(a). For a constant C_p, the 3D numerical model predicts values very close to the analytical results. When the full $C_p(T)$ is used, the 3D model predicts $T(t)$ remarkably close to the experiments. This feature underlines the ability of the numerical model to cope with the non-linearities of $C_p(T)$ and gives evidence that the irregular behavior in the experimental $T(t)$ is closely related to $C_p(T)$.

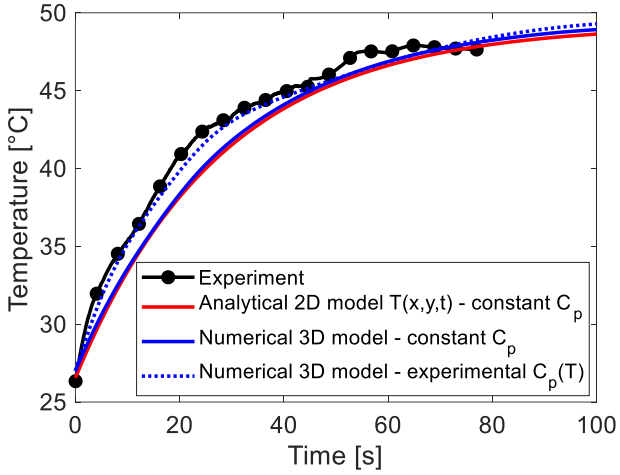

Figure 6: Temperature evolution with time measured experimentally (black dots), analytically as per section 2.2 (red) and numerically (blue lines). Comparison between constant and temperature-dependent C_p.

Figure 7 shows the steady-state temperature distribution $T_s(x, y)$ on a quarter of the cross-section of the SMC calculated analytically either by equation 6 (constant electrical resistivity) or equation 18 (temperature-dependent electrical resistivity) including the GCF. The $T(x, y)$ predicted by the Ansys model in a central slice of the 3D geometry is also shown (either at constant ρ_0 or using the experimental $\rho_e(T)$ in Figure 4(b)). As it can be seen in Figure 7, the analytical model with temperature-dependent resistivity is quite close to the case of constant resistivity (equation 6). The predicted temperature distribution using the 3D Ansys model at constant resistivity displays a very similar steady-state temperature distribution than the above two analytical calculations including the GCF. This small difference confirms the assumption of infinite length in the 2D analytical formulas for geometries such as the one presented in this study. When the experimental $\rho_e(T)$ is considered in the 3D model, the maximum difference with the constant resistivity modelling is 2.1 ºC, i.e. less than 4.3%, although resistivity changes of ~10% are observed during resistive heating. This can be explained by the small change of local dissipated power caused by a finite temperature coefficient α when the resistive

heating is carried out at constant power. As equation 16 shows in the particular case of a linear T dependence, the relative change in the dissipated power is $\alpha[T(x,y)-\langle T\rangle]$. As a consequence, the temperature range to be considered is the difference between the local temperature and its average over the cross-section, and not the whole temperature increase. An upper bound of this change is given approximately by $\alpha\,(q_0 ab)/(2\kappa)$.

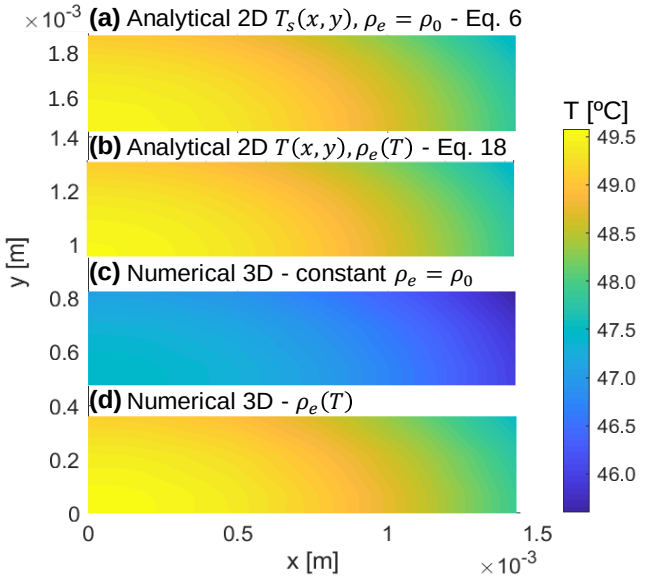

Figure 7: Steady-state temperature distribution on a quarter of a slice of the SMC: (a) analytical results for non-uniform temperature distribution and temperature-independent resistivity (equation 6) with GCF, (b) with temperature dependent resistivity (equation 18) with GCF, (c) the numerical results at the central slice of the 3D thermoelectric model in Ansys with constant resistivity and (d) with the experimental temperature-dependent resistivity.

Figure 8 compares the surface steady-state temperature distribution $T_s(x,b)$ along the width of the SMC sample $(-a \le x \le a)$: experimental, analytical and numerical results. The experimental values (given in black circles) follow a distinguishable parabolic shape with minimum and maximum values $T_s(a,b) =$ 46.1 ºC and $T_s(0,b) =$ 49.7 ºC. The numerical (in blue) and the analytical results (in red) are plotted for different values of κ: the average measured of 0.22 W·m^{-1}·K^{-1} and the best fit of 0.11 W·m^{-1}·K^{-1} (found using the approximation in equation 13 on the experimental results). Varying κ changes the temperature distribution considerably but the average value stays almost unchanged. Results plotted in Figure 8 give evidence that the best fit of the surface temperature distribution is obtained for a much lower κ than that obtained by independent measurements on similar materials, both differing only by 0.11 W·m^{-1}·K^{-1}. A possible explanation of the small difference between the numerical model and the experiments is that the κ measurements in this work are obtained around room temperature, while the average temperature in Figure 8 is ~ 48 °C. As previously reported in [27] , the temperature coefficient of the thermal conductivity is negative for these type of materials and hence the actual κ of the SMC at 48 ºC will be smaller than the measured at room temperature. This agrees with the estimated κ of 0.11 W·m^{-1}·K^{-1} found analytically. In spite of this discrepancy, both numerical and analytical models are shown to be able to reproduce the parabolic distribution obtained experimentally. In particular, equation 14 can be used to estimate κ from a resistive heating experiment of the SMC material.

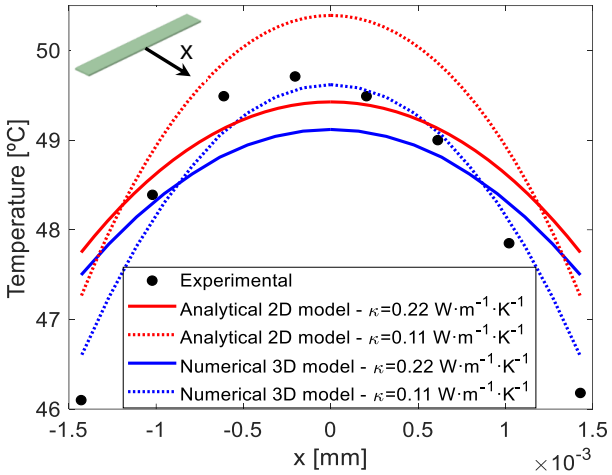

Figure 8: Experimental steady-state temperature on the center line at the surface of the SMC (in black) compared to the analytical (in red) and numerical (in blue) results for two values of thermal conductivity.

5.4 Resistive heating results on the "SMC with grips"

When trying to measure or make use of the shape memory properties of SMC, one needs to be able to deform the sample. With that aim, practically, the SMC is attached to external bodies that will influence the resistive heating of the samples. In order to study the influence of these fixing structures, the experimental resistive heating results of both geometries (i.e. "bare SMC" and "SMC with grips") are shown in Figure 9 for another sample with the same geometry and experimental conditions as before. These measurements were both carried out at the same input power of 0.1 W and yet it is possible to see that the addition of the grips on the set-up noticeably changes both the transient and the steady-state temperature due to resistive heating. Resistive heating with grips leads to a lower steady-state temperature upon the injection of the current. This is due to the additional heat dissipation from the surface of the samples to the grips by conduction. The fact that this conduction heat transfer occurs is also the explanation for the slower resistive heating phenomenon since the grips function as a heat sink with an added thermal mass. These results give evidence that the presence of grips for mechanical experiments on the SMC may affect considerably the resistive heating behavior. The results of Figure 9 also show that the

influence of the grips on the transient $T(t)$ can be modelled successfully.

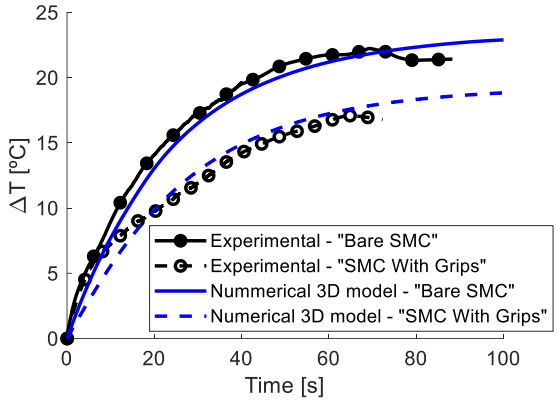

Figure 9: Average temperature evolution with time on the surface of the SMC sample "Bare SMC" (solid line) and "SMC with grips" (dashed line): experimental results in black and numerical results in blue.

6. Conclusions

A comprehensive analysis of the resistive heating of SMC when subjected to the injection of an electric current at constant power is investigated. The experimental temperature measured on the surface of the SMC parallelepiped samples is compared to analytical and numerical models that couple both the thermal and the electrical phenomena. The findings shown in this article can be summarized as follows:

i. The electrical resistivity of this SMC has a non-linear dependence on temperature, exhibiting a maximum at the melting temperature of the polymer. For controlled resistive heating of the SMC at constant power, the injected current needs to continuously vary.

ii. A simple analytical 1D model assuming temperature homogeneity within the samples serves to have a good first approximation of the resistive heating phenomenon. Nevertheless, the final steady-state temperature is somewhat underestimated.

iii. The transient 2D analytical model with temperature-independent resistivity developed in this study predicts a resistive heating phenomenon closer to the experimental data than the 1D model. The difference between the 2D analytical model with temperature-independent resistivity and the 1D analytical model resides in the additional temperature gradients that arise due to the finite value of the thermal conductivity. This analytical 2D model can be used for predicting the resistive heating arising from the injection of a current at constant power without the need of numerical modelling. Furthermore, parametric investigations of the variations of certain geometrical and material properties can be done easily and rapidly for a sample with rectangular cross-section, e.g. a metal (positive α) or even a semiconductor (negative α), provided the assumptions of the calculations are met and a constant α can be assumed within the temperature range considered.

iv. The 2D analytical models and the 3D numerical model in Ansys predict elliptic temperature distributions in the XY-plane, consistent with the type of distribution found experimentally on the SMC surface.

v. Simpler analytical expressions are derived for the frequent case of Biot number much smaller than unity: these results permit the prediction, for any dimension or range of parameters, of the magnitude of the thermal gradients within the sample or, in an equivalent manner, find an upper bound of the sample dimensions that lead to a certain maximum temperature difference (e.g. 1 ºC) within the sample.

vi. For the first time, the 2D local dissipated power due to the injection of an electric current at constant power has been described (in equation 16) for a material exhibiting a linear temperature dependence of resistivity. The practical consequence is that the temperature difference that is relevant to estimate the effect of a finite temperature coefficient α is not the average temperature increase $(T(x,y) - T_0)$ but the local temperature non-uniformity $(T(x,y) - \langle T \rangle)$.

vii. Several material parameters have been shown to heavily influence the resistive heating of SMC upon the injection of a current at constant power. These are:

   a. temperature-dependent resistivity: when the resistivity is no longer considered constant but temperature-dependent, the 2D steady-state analytical model is modified so that the local dissipated power follows a linear temperature dependence. This model is shown to be successfully applied to approximate the non-linear temperature dependence of the resistivity in a piece-wise linear fashion. The results have shown that neglecting the temperature-dependent resistivity may result in temperatures that are much lower than those intended. Therefore, for applications such as shape memory cycles, in which a certain temperature (the transition temperature) needs to be reached, the knowledge and description within the analytical model of the material's temperature-dependent resistivity is needed.

   b. temperature-dependent heat capacity: using a constant heat capacity throughout the analytical models results in slower resistive heating phenomena than the experiment. However, when describing the non-linear temperature dependence of the heat capacity in the 3D numerical model in Ansys, the resulting numerical temperature evolution with time is a very close match with the experiment. Hence, this result highlights the importance of including such a non-monotonic temperature dependence of the heat capacity for an

accurate prediction of the transient characteristics of the resistive heating phenomenon.

c. thermal conductivity: the higher the value of thermal conductivity, the lower the temperature differences within the sample. However, the average temperature within the sample stays almost constant regardless of the value of thermal conductivity. An average value of $\kappa = 0.22$ $W{\cdot}m^{-1}{\cdot}K^{-1}$ is measured. Furthermore, an inverse identification of κ based on the experimental surface temperature measurements results in a smaller κ, but having the same order of magnitude (0.11 $W{\cdot}m^{-1}{\cdot}K^{-1}$). The results presented in this paper highlight the importance of characterizing the thermal conductivity for predicting the temperature distribution in SMC in which heating is produced by an electric current.

viii. When trying to use the SMC with realistic conditions, the resistive heating phenomenon may be drastically different depending on the structures that are placed in contact. This study has shown that, when attached by grips intended to apply a certain deformation within the shape memory cycle, a great thermal mass is added. This yields a slower resistive heating and lower steady-state temperatures than for the "bare SMC". If a certain temperature needs to be reached with resistive heating, the influence of these type of structures must be taken into account.

Acknowledgements

The research was founded through the "Actions de recherche concertées 2017 - Synthesis, Characterization, and MultiScale Model of Smart composite Materials (S3CM3) 17/21-07'' financed by the "Direction générale de l'Enseignement non obligatoire de la Recherche scientifique, Direction de la Recherche scientifique, Communauté française de Belgique, et octroyées par l'Académie Universitaire Wallonie-Europe".

References

[1] Melly S K, Liu L, Liu Y and Leng J 2020 *J. Mater. Sci.* **55** 10975-11051
[2] Behl M and Lendlein A 2007 *Soft Matter* **3** 58-67
[3] Xin X, Liu L, Liu Y and Leng J 2019 *Acta Mech. Solid. Sin.* **32** 535
[4] Gong X, Liu L, Liu Y and Leng J 2016 *Smart Mater. Struct.* **25** 035036
[5] Eisenhaure J and Kim S 2014 *Polymers* **6** 2274-2286
[6] Soto G D, Meiorin C, Actis D G, Mendoza Zélis P, Moscoso Londono O, Muraca D, Mosiewicki M A and Marcovich N E 2018 *Eur. Polym. J.* **109**, 8-15
[7] Ze A, Kuang X, Wong J, Macrae Montgomery S, Zhang R, Kovitz J M, Yang F, Qi J and Zhao R 2020 *Adv. Mater.* **32** 1906657
[8] Tian G, Zhu G, Xu S and Pan L 2020 *Smart Mater. Struct.* **29** 105019
[9] Herath M, Epaarachchi J, Islam M, Fang L and Leng J 2020 *Eur. Polym. J.* **136** 109912
[10] Li Y, Chen H, Liu D, Wang W, Liu Y and Whou S 2015 *ACS Appl. Mater. Interfaces* **7** 12988-12999
[11] Song Q, Chen H, Zhou S, Zhao K, Wang B and Hu P 2016 Polym. Chem. **7** 1739
[12] Arun D I, Chakravarthy P, Girish B S, Santhosh Kumar K S and Santhosh B 2019 *Smart Mater. Struct.* **28** 055010
[13] Park J H, Dao T D, Lee H, Jeong H M and Kim B K 2014 *Materials* **7** 1520-1538
[14] Datta S, Henry T C, Sliozberg Y R, Lawrence B D, Chattopadhyay A and Hall A J 2021 *Polymer* **212** 123158
[15] Tarfaoui M, El Moumen A, Boehle M, Shah O and Lafdi K 2019 *J. Mater. Sci.* **54**, 1351-1362
[16] Chen H, Zhang F, Sun Y, Sun B, Gu B, Leng J and Zhang W 2021 *Smart Mater. Struct.* **30** 025040
[17] Yenpech N, Intasanta V and Chirachanchai S 2019 *Polymer* **182** 121792
[18] El Moumen A, Tarfaoui M, Nachtane M and Lafdi K 2019 *Compos. B.* **164** 67-71
[19] Tarfaoui M, El Moumen A, Lafdi K, Hassoon O H and Nachtane M 2018 *J. Compos. Mater.* **52** 3655-3667
[20] Leng J, Lan X, Liu Y and Du S 2009 *Smart Mater. Struct.* **18** 074003
[21] Taherian R and Matboo Ghorbani M 2017 *ECS J Solid State Sci. Technol.* **6** 3019-3027
[22] VanSant J H *Conduction Heat Transfer Solutions*, 1980, United States, doi:10.2172/7035199
[23] Carslaw H S and Jaeger J C *Conduction of Heat in Solids*, Oxford: Clarendon Press, 1959, 2nd ed.
[24] Ansys Inc., *Mechanical Application 2020 R1: Mechanical User's Guide* 2020
[25] Defize T, Thomassin J M, Alexandre M, Gilbert B, Riva R and Jérôme C 2018 *Polym.* **84** 234
[26] Fagnard J F, Stoukatch S, Laurent P, Dupont F, Wolfs C Lambert S D and Redouté J M 2021 *IEEE Trans. Compon. Packaging Manuf. Technol.***4** 606
[27] Wurm A, Lellinger D, Minakov A A, Skipa T, Pötschke P, Nicula R, Alig I and Schick C 2014Polym.**9** 2220-2232
[28] Karwa R *Heat and Mass Transfer*, Springer, 2020, 2nd ed.

Appendix I: Nusselt and radiation-equivalent Nusselt number calculation.

- The Nusselt number (Nu) is a dimensionless parameter defined as the ratio between the convective and the conductive heat transfer [28]. Nu > 10 means that convection dominates conduction during the heat transfer from the solid sample to the surroundings and therefore conduction heat transfer from the solid to the ambient can be neglected. For the problem described in this study where the parallelepiped samples are suspended vertically, the Nusselt number can be defined as

$$\mathrm{Nu} = \frac{hL}{\kappa_{air}} \qquad \text{(A1)}$$

where h is the convection coefficient (i.e. for the material in this study $h \approx 25$ W·m^{-2} K^{-1}), L is the length of the sample (characteristic length for the convection phenomenon, for the samples in this study $L = 25$ mm) and κ_{air} is the thermal conductivity of air at the characteristic temperature of the boundary layer T_{BL}. This characteristic temperature, for the data presented in this article, can be estimated to be $T_{BL} \approx (T_{max} + T_0)/2 \approx 37.2$ ºC (where T_{max} and T_0 are the maximum and the initial temperature respectively). At this temperature, $\kappa_{air} \approx 0.027$ W·m^{-1}·K^{-1}. Substituting these values into the definition of Nu one gets Nu ≈ 23. Therefore, the conduction heat transfer from the sample to the surroundings can be neglected over convection.

- The radiation-equivalent Nusselt number (Nu_r) is a dimensionless parameter that can be defined as the ratio of the heat transferred through radiation and the heat transferred through convection:

$$\mathrm{Nu}_r = \frac{Q_{rad}}{Q_{conv}} = \frac{\sigma \varepsilon A_T (T^4 - T_0^4)}{h A_T (T - T_0)} \qquad \text{(A2)}$$

where σ is the Stephan-Boltzmann constant, ε the emissivity of the material (measured to be 0.91), and A_T the total area as defined in the article. The Nu_r for these samples is $\mathrm{Nu}_r \approx 4.6 \cdot 10^{-4}$. Since $\mathrm{Nu}_r \ll 1$, radiation heat transfer can be neglected when compared to convection heat transfer.

Appendix II: Derivation of the transient temperature term included in the analytical 2D model describing the resistive heating of a sample with non-uniform temperature and temperature-independent resistivity.

Let us assume that the sample is a parallelepiped of length L, width $2a$ and thickness $2b$ such that $L \gg a \gg b$ and a coordinate system centered on its cross-section $-a \leq x \leq a$ and $-b \leq y \leq b$. In the 2D approximation, the sample exhibits a total non-uniform temperature distribution $T(x,y,t)$ in its cross-section arising due to the resistive heating produced by the injection of an electric current parallel to the length L. The material is assumed to have a constant electrical resistivity ρ_0 and a finite thermal conductivity κ. All surfaces of the parallelepiped are subjected to free convection cooling as defined by Newton's law of cooling and the heat transfer by conduction and radiation to the surroundings is neglected. At the beginning of the resistive heating phenomenon, the sample is at a uniform temperature that is equal to the temperature of the surroundings (T_0).

The total temperature distribution can be described as the addition of a steady-state temperature $T_s(x,y)$ and a transient part $T_t(x,y,t)$ that depends on time t. The former has already been published by Carslaw and Jaeger [20]. The solution, expressed as a function of the variables used throughout this paper, is the following:

$$T_s(x,y) = T_0 + \frac{aq_0}{h}\left(1 + \frac{\mathrm{Bi}}{2}\left(1 - \left(\frac{x}{a}\right)^2\right)\right) - \frac{4q_0 a}{h}\sum_{n=1}^{\infty}\frac{\mathrm{Bi}\sin(\Lambda_n)\cos\left(\Lambda_n\frac{x}{a}\right)\cosh\left(\Lambda_n\frac{y}{a}\right)}{\Lambda_n^2[2\Lambda_n + \sin(2\Lambda_n)]\left[\frac{\Lambda_n}{\mathrm{Bi}}\sinh\left(\Lambda_n\frac{b}{a}\right) + \cosh\left(\Lambda_n\frac{b}{a}\right)\right]} \quad \text{(A3)}$$

where q_0 is the dissipated power per unit volume and $\Lambda_n \tan(\Lambda_n) = \frac{ha}{\kappa} = \mathrm{Bi}$, Bi standing for the Biot number.

The step-by-step solution to the transient part $T_t(x,y,t)$ is given hereinafter.

The 2D transient heat transfer governing equation for this problem is

$$\frac{\partial^2 T_t(x,y,t)}{\partial x^2} + \frac{\partial^2 T_t(x,y,t)}{\partial y^2} = \frac{\rho_m C_p}{\kappa}\frac{\partial T_t(x,y,t)}{\partial t} \quad \text{(A4)}$$

where ρ_m is the density of the material and C_p the heat capacity. The boundary conditions for this transient problem applying symmetry along the x and y axis are the following:

$$\frac{\partial T_t}{\partial x} = 0 \qquad \forall \ x = 0 \quad \text{(A5)}$$

$$\kappa\frac{\partial T_t}{\partial x} + h(T_t) = 0 \qquad \forall \ x = +a \quad \text{(A6)}$$

$$\frac{\partial T_t}{\partial y} = 0 \qquad \forall \ y = 0 \quad \text{(A7)}$$

$$\kappa\frac{\partial T_t}{\partial y} + h(T_t) = 0 \qquad \forall \ y = +b \quad \text{(A8)}$$

The initial condition for this problem states that $T_t(x,y,t=0) = T(x,y,t=0) - T_s(x,y) = T_0 - T_s(x,y)$.

Applying separation of variables such that $T_t(x,y,t) = V(x,y)Z(t)$, one will obtain a temporal and a spatial problem separately such that

$$\frac{\rho_m C_p}{\kappa}\frac{\dot{Z}}{Z} = \frac{\frac{\partial^2 V}{\partial x^2} + \frac{\partial^2 V}{\partial y^2}}{V} = \beta \tag{A9}$$

where β is a constant.

A. Solution to the spatial problem $\frac{\partial^2 V}{\partial x^2} + \frac{\partial^2 V}{\partial y^2} = V\beta$:

Applying the separation of variables for a second time, $V(x,y) = P(x)Q(y)$. Substituting inside the spatial problem characteristic equations, one gets

$$\frac{\ddot{P}}{P} = \beta - \frac{\ddot{Q}}{Q} = -\mu^2 \tag{A10}$$

where μ is a constant. The solution to the ordinary differential equations for $P(x)$ (i.e. $\ddot{P} + \mu^2 P = 0$) and $Q(y)$ (i.e. $\ddot{Q} - (\beta + \mu^2)Q = 0$) is straightforward and can be expressed as

$$P(x) = D_1 \cos(\mu x) + D_2 \sin(\mu x) \tag{A11}$$

The coefficients D_i are constants to be determined with the boundary conditions. Applying the first boundary condition in equation A11 at $x = 0$, the coefficients D_2 vanishes in order to avoid trivialities.

A.1. Case in which $\beta < -\mu^2$:

If $\beta < -\mu^2$ once can introduce the parameter η such that $\eta^2 = -(\beta + \mu^2)$. The spatial term $Q(y)$ has the form

$$Q(y) = D_3 \cos(\eta y) + D_4 \sin(\eta y) \tag{A12}$$

The coefficients D_i are constants to be determined with the boundary conditions. Applying the third boundary condition in equation A12 at the center $y = 0$, the coefficient D_4 vanishes in order to avoid trivialities. Using the second boundary condition of equation A6, one gets the transcendental equation

$$\mu_m a \tan(\mu_m a) = \frac{ha}{\kappa} = \mathrm{Bi} \tag{A13}$$

By introducing $\mathrm{M}_m = \mu_m a$, equation A13 can be expressed as $\mathrm{M}_m \tan(\mathrm{M}_m) = \mathrm{Bi}$.

The 4th boundary condition (equation A8) yields yet another similar transcendental equation:

$$\eta_l b \tan(\eta_l b) = \frac{hb}{\kappa} = \mathrm{Bi}\frac{b}{a} \tag{A14}$$

By introducing the dimensionless number $\mathrm{H}_l = \eta_l b$, equation A14 can be expressed as $\mathrm{H}_l \tan(\mathrm{H}_l) = \mathrm{Bi}\, b/a$.

The solution to the spatial problem $V(x,y)$ would therefore remain as a double series of addition where the constants D_1 and D_3 can be combined into a single constant $D_{5,ml}$. The expression for $V(x,y)$ is the following:

$$V(x,y) = \sum_{m=1}^{\infty}\sum_{l=1}^{\infty} D_{5,ml} \cos\left(\mathrm{M}_m \frac{x}{a}\right) \cos\left(\mathrm{H}_l \frac{x}{b}\right) \tag{A15}$$

A.2. Case in which $\beta > -\mu^2$:

If $\beta > -\mu^2$ one can introduce the parameter η such that $\eta^2 = (\beta + \mu^2)$. In what follows, it is shown that this case will not be mathematically possible. Consider that η can be defined as above. Then the spatial term $Q(y)$ would have the form

$$Q(y) = \widetilde{D}_3 \cosh(\eta y) + \widetilde{D}_4 \sinh(\eta y) \tag{A16}$$

where the coefficients $\widetilde{D}_i$ can be found using the boundary conditions. Applying the third boundary condition (equation A7), one gets $\widetilde{D}_4 = 0$, and applying the fourth boundary condition (equation A8) one gets $\kappa\eta\widetilde{D}_3 \sinh(\eta b) + h\widetilde{D}_3 \cosh(\eta b) = 0$. This expression can be re-written as:

$$\eta b \tanh(\eta b) = -\frac{hb}{\kappa} = -\mathrm{Bi}\frac{b}{a} \tag{A17}$$

If one introduces again $\mathrm{H} = \eta b$, equation A17 can be expressed as $\mathrm{H}\tanh(\mathrm{H}) = -\mathrm{Bi}\, b/a$. Since $\mathrm{Bi}\, b/a > 0$, the only solution for H must be imaginary, i.e. H should take the form $\mathrm{H} = j|\mathrm{H}|$, where $j = \sqrt{-1}$.

In this case, β would take the form $\beta_m = \left(\frac{\mathrm{H}}{b}\right)^2 - \left(\frac{\mathrm{M}_m}{a}\right)^2$. Since $\left(\frac{\mathrm{H}}{b}\right)^2$ is a negative value because H is imaginary, the statement done at the beginning of $\beta > -\mu^2$ is not true and this case cannot happen.

B. Solution to the temporal problem $\frac{\rho_m C_p}{\kappa}\frac{\dot{Z}}{Z} = \beta$:

Taking into account that the constant β can be expressed in terms of the constants derived above in case A.1 (i.e. $\beta_{ml} = -(\mu_m^2 + \eta_l^2)$), the solution to the ordinary differential equation is simply:

$$\dot{Z} + \frac{\kappa}{\rho C_p}(\mu_m^2 + \eta_l^2)Z = 0 \rightarrow Z_{ml}(t) = D_{6,ml} \exp\left(-\frac{\kappa}{\rho C_p}(\mu_m^2 + \eta_l^2)t\right) \tag{A18}$$

where $D_{6,ml}$ is a constant.

Thanks to the solution of both the spatial and the temporal problems, the complete solution for the transient part is the multiplication of these last two equations. The result of the transient part is:

$$T_t(x,y,t) = \sum_{m=1}^{\infty}\sum_{l=1}^{\infty} C_{3,ml} \cos\left(\mathrm{M}_m \frac{x}{a}\right) \cos\left(\mathrm{H}_l \frac{x}{b}\right) \exp\left(-\frac{\kappa}{\rho C_p}(\mu_m^2 + \eta_l^2)t\right) \tag{A19}$$

where $C_{3,ml}$ is a constant that results from the multiplication of $D_{5,ml}$ and $D_{6,ml}$. After applying the initial condition on $T_t(x,y,t)$ one gets

$$T_0 - T_s(x,y) = \sum_{m=1}^{\infty}\sum_{l=1}^{\infty} C_{3,ml}\cos\left(\mathrm{M}_m\frac{x}{a}\right)\cos\left(\mathrm{H}_l\frac{y}{b}\right) \tag{A20}$$

To solve for $C_{3,ml}$, one can take advantage of the orthogonality of the eigenfunctions and multiply both sides by $\cos(\mathrm{M}_k x/a)\cdot\cos(\mathrm{H}_j y/b)$ and integrate over the cross-section. Due to this orthogonality, there is a solution only if $\mathrm{M}_m = \mathrm{M}_k$ and H_l=H_j. Furthermore, one may notice that the coefficients m and n must be equal. This implies that $\mathrm{M}_m = \Lambda_n$. The left-hand side of the equation would therefore remain as:

$$\begin{aligned}\mathrm{C}_{2,nl} &= \int_{-a}^{a}\int_{-b}^{b}[T_0 - T_s(x,y)]\cos\left(\mathrm{M}_m\frac{x}{a}\right)\cos\left(\mathrm{H}_l\frac{y}{b}\right)dydx = \\ &= -\frac{4a^2 b q_0\sin(\mathrm{H}_l)\left[(\Lambda_n^2+\mathrm{Bi})\sin(\Lambda_n)-\Lambda_n\mathrm{Bi}\cos(\Lambda_n)\right]}{h\Lambda_n^3\mathrm{H}_l} \\ &+ \frac{4q_0 a^3\mathrm{Bi}\sin(\Lambda_n)\left(\Lambda_n\sinh\left(\Lambda_n\frac{b}{a}\right)\cosh(\mathrm{H}_l)+\frac{a}{b}\mathrm{H}_l\cosh\left(\Lambda_n\frac{b}{a}\right)\sin(\mathrm{H}_l)\right)}{h\Lambda_n^3\left[\frac{\Lambda_n}{\mathrm{Bi}}\sinh\left(\Lambda_n\frac{b}{a}\right)+\cosh\left(\Lambda_n\frac{b}{a}\right)\right]\left[\Lambda_n^2+\mathrm{H}_l^2\left(\frac{a}{b}\right)^2\right]}\end{aligned} \tag{A21}$$

By solving for $C_{3,nl}$ one obtains:

$$C_{3,nl} = \frac{4\Lambda_n\mathrm{H}_l\,C_{2,nl}}{ab[2\Lambda_n+\sin(2\Lambda_n)][2\mathrm{H}_l+\sin(2\mathrm{H}_l)]} \tag{A22}$$

Once the coefficients $C_{2,nl}$ and $C_{3,nl}$ are defined, the transient part of the temperature distribution has a closed solution:

$$T_t(x,y,t) = \sum_{n=1}^{\infty}\sum_{m=1}^{\infty} C_{3,nl}\cos\left(\Lambda_n\frac{x}{a}\right)\cos\left(\mathrm{H}_l\frac{y}{b}\right)*\exp\left(-\frac{\kappa}{\rho_m C_p}\left(\frac{\Lambda_n^2}{a^2}+\frac{\mathrm{H}_l^2}{b^2}\right)t\right) \tag{A23}$$

Appendix III: Derivation of the approximation of steady-state non-uniform temperature and temperature-independent resistivity for Bi << 1 (equation 13 of the main body of the article)

In order to approximate the steady-state temperature distribution of equation 6 of the main body of the article for cases of Bi << 1, one starts by approximating the roots of Λ_n given in equation 7 of the main body of the article. The roots of Λ_n can be approximated as

$$\Lambda_n \approx \begin{cases} \sqrt{\mathrm{Bi}} & \text{for } n = 1 \\ (n-1)\pi + \dfrac{\mathrm{Bi}}{(n-1)\pi} & \forall\ n > 1 \end{cases} \qquad \text{(A24)}$$

When Bi << 1, the Λ_1 of the equation satisfies also Λ_1 << 1 and can be approximated by $\Lambda_1 \tan(\Lambda_1) \approx (\Lambda_1)^2 = \mathrm{Bi}$, i.e. $\Lambda_1 \approx \mathrm{Bi}^{1/2}$. The following roots are very close to $(n-1)\pi$, i.e. can be expressed as $\Lambda_n \approx (n-1)\pi + \varepsilon_n$ with ε_n << 1. Substituting in equation 7 one finds $\varepsilon_n \approx Bi/[(n-1)\pi]$, i.e. the result shown in equation A24. In such case, the first term of the series in equation 6 dominates and the others can be neglected.

Using the assumption Bi << 1 and taking into account that Λ_1 is also much smaller than 1, one can use the Taylor series expressions for the trigonometric and hyperbolic functions in equation 6. Restricting the expansion of $T_s(x, y)$ to the second order in Λ_1, the approximation in equation 13 of the main body of the article is obtained.

Appendix IV: Derivation of the expression for the 2D local dissipated power arising due to resistive heating upon the injection of an electric current at constant power through a material exhibiting a linear temperature dependence of resistivity.

Let us assume that the sample is a parallelepiped of length L, width $2a$ and thickness $2b$ such that $L \gg a \gg b$ and a coordinate system centered on its cross-section $-a \leq x \leq a$ and $-b \leq y \leq b$. In the 2D approximation, the sample exhibits non-uniform temperature distribution $T(x,y)$ in its cross-section arising due to the resistive heating produced by the injection of an electric current passing through. If the electrical resistivity of the sample is temperature dependent, then it is also non-uniform $\rho_e = \rho_e[T(x,y)]$. For that reason, even if the current is injected at constant power, the local dissipated power $q(x,y)$ will also be non-uniform because the current will redistribute to preferably flow throw the paths of least resistivity.

The local dissipated power is the product of the local current density $J(x,y)$ and the local electric field $E(x,y)$. By making use of Ohm's law ($E = \rho_e J$), the local dissipated power can be expressed in terms of the local resistivity as $q(x,y) = \frac{E^2}{\rho_e(x,y)}$. If the sample is assumed to have a uniform cross-section, the electric field can be assumed to be $E = \frac{V}{L}$, where V is the total voltage across the sample. Furthermore, at constant power P_0, the total voltage is defined as $V^2 = P_0 R(T)$, where $R(T)$ is the total resistance of the sample that is related to the infinite number of parallel current paths of cross-section $\mathrm{d}x\ \mathrm{d}y$ and resistivity $\rho_e(x,y)$. The conductance of these paths can be defined as $\mathrm{d}G(x,y) = \frac{\mathrm{d}x\ \mathrm{d}y}{L\ \rho_e(x,y)}$. The total conductance ($G = R^{-1}$) is the integral over the cross-section of the sample. The total resistance of the sample is therefore given by

$$R(T) = \frac{L}{\int_{-a}^{a}\int_{-b}^{b} \frac{\mathrm{d}x\mathrm{d}y}{\rho_e\ (x,y)}} \tag{A25}$$

The local dissipated power $q(x,y)$ can then be expressed in terms of P_0 and $\rho_e(x,y)$ as

$$q(x,y) = \frac{P_0}{\rho_e(x,y)\ L\ \int_{-a}^{a}\int_{-b}^{b} \frac{\mathrm{d}x\mathrm{d}y}{\rho_e(x,y)}} = \frac{q_0\ (4ab)}{\rho_e(x,y)\ \int_{-a}^{a}\int_{-b}^{b} \frac{\mathrm{d}x\mathrm{d}y}{\rho_e(x,y)}} \tag{A26}$$

where q_0 denotes the average power per unit volume ($q_0 = P_0/(4Lab)$)

Let us assume that the resistivity varies linearly with temperature as per $\rho_e(T) = \rho_0[1 + \alpha(T - T_0)]$, where α is the temperature coefficient of resistivity (units of K^{-1}), T_0 is the temperature of the surroundings and ρ_0 the resistivity of the sample at said temperature. Moreover, one can assume that the local resistive heating is kept moderate such that $\alpha(T - T_0) \ll 1$. Doing so, the local resistive heating $q(x,y)$ can be approximated as:

$$q(x,y) = \frac{q_0\,(4ab)}{\frac{\rho_e(x,y)}{\rho_0}\int_{-a}^{a}\int_{-b}^{b}\frac{\mathrm{d}x\mathrm{d}y}{1+\alpha[T(x,y)-T_0]}} \approx \frac{q_0\,(4ab)}{\frac{\rho_e(x,y)}{\rho_0}\int_{-a}^{a}\int_{-b}^{b}\{1-\alpha[T(x,y)-T_0]\}\mathrm{d}x\mathrm{d}y} \tag{A27}$$

The integral term in the denominator can be left in terms of the average temperature within the sample $\langle T(x,y)\rangle$, i.e. $\int_{-a}^{a}\int_{-b}^{b}\{1-\alpha[T(x,y)-T_0]\}\mathrm{d}x\mathrm{d}y = 4ab\{1-\alpha[\langle T(x,y)\rangle - T_0]\}$. Finally, substituting this expression into the local heat dissipation and further applying the approximations abovementioned:

$$q(x,y) \approx \frac{q_0}{\{1+\alpha[T(x,y)-T_0]\}\{1-\alpha[\langle T(x,y)\rangle - T_0]\}} \approx q_0\{1-\alpha[T(x,y)-\langle T(x,y)\rangle]\} \tag{A28}$$

Appendix V: Derivation of the steady-state 2D temperature field describing the resistive heating of a sample with non-uniform temperature and temperature-dependent resistivity $\rho_e(T)$.

Let us assume that the sample is a parallelepiped of length L, width $2a$ and thickness $2b$ such that $L \gg a \gg b$ and a coordinate system centered on its cross-section $-a \leq x \leq a$ and $-b \leq y \leq b$. In the 2D steady-state approximation, the sample exhibits a total non-uniform temperature distribution $T(x,y)$ in its cross-section arising due to the resistive heating produced by the injection of an electric current passing through. The material is assumed to have finite thermal conductivity κ and a temperature-dependent electrical resistivity $\rho_e(T)$ such that $\rho_e(T) = \rho_0[1 + \alpha(T - T_0)]$, where ρ_0 is the electrical resistivity at the room temperature T_0. All surfaces of the parallelepiped are subjected to free convection cooling as defined by Newton's law of cooling and the heat transfer by conduction and radiation to the surroundings is neglected.

Due to that linear temperature dependence on resistivity, the local heat dissipation $q(x,y)$ would be given by equation A28. The heat balance equation would then be

$$\frac{\partial^2 T(x,y)}{\partial x^2} + \frac{\partial^2 T(x,y)}{\partial y^2} - \frac{q_0 \alpha}{\kappa} T(x,y) = -\frac{q_0}{\kappa}(1 + \alpha\langle T(x,y)\rangle) \tag{A29}$$

with the boundary conditions

$$\begin{aligned} &\frac{\partial T}{\partial x} = 0 && \forall \;\; x = 0 \\ &\kappa\frac{\partial T}{\partial x} + h(T - T_0) = 0 && \forall \;\; x = +a \\ &\frac{\partial T}{\partial y} = 0 && \forall \;\; y = 0 \\ &\kappa\frac{\partial T}{\partial y} + h(T - T_0) = 0 && \forall \;\; y = +b \end{aligned} \tag{A30}$$

To solve this non-homogeneous partial differential equation there is several methods that one can follow. As an example, the temperature field $T(x,y)$ can take the form $T(x,y) = \phi(x) + \varphi(x,y)$ so that equations A29 and A30 can be split up into a non-homogeneous ordinary differential equation depending on x, i.e. equation A31 with its boundary conditions in A32

$$\frac{d^2\phi}{dx^2} - \frac{q_0 \alpha}{\kappa}\phi = -\frac{q_0}{\kappa}(1 + \alpha\langle T(x,y)\rangle) \tag{A31}$$

$$\begin{aligned} &\frac{d\phi}{dx} = 0 && \forall \;\; x = 0 \\ &\kappa\frac{d\phi}{dx} + h(\phi - T_0) = 0 && \forall \;\; x = +a \end{aligned} \tag{A32}$$

and a homogeneous partial differential equation depending on y (equation A33 with its boundary conditions in equation A34).

$$\frac{\partial^2 \varphi}{\partial x^2} + \frac{\partial^2 \varphi}{\partial y^2} - \frac{q_0 \alpha}{\kappa}\varphi = 0 \tag{A33}$$

$$\begin{aligned} \frac{\partial \varphi}{\partial x} &= 0 && \forall \quad x = 0 \\ \kappa \frac{\partial \varphi}{\partial x} + h\varphi &= 0 && \forall \quad x = +a \\ \frac{\partial \varphi}{\partial y} &= 0 && \forall \quad y = 0 \\ \kappa \frac{\partial \varphi}{\partial y} + h(\varphi + \phi - T_0) &= 0 && \forall \quad y = +b \end{aligned} \tag{A34}$$

The solution of equation A31 is

$$\phi(x) = \frac{1 + \alpha\langle T(x,y)\rangle}{\alpha} + D_7 \exp\left(\sqrt{\frac{q_0\alpha}{\kappa}}x\right) + D_8 \exp\left(-\sqrt{\frac{q_0\alpha}{\kappa}}x\right) \tag{A35}$$

where D_7 and D_8 can be obtained thanks to the boundary conditions in A32. Doing so, the first boundary condition gives $D_7 = D_8$, and therefore the exponential terms can be gathered together in terms of a hyperbolic cosine $C_4\cosh(x\sqrt{((q_0\alpha)/\kappa)})$ where $C_4 = 2D_7$. The second boundary condition in equation A32 gives a solution for C_4 such that

$$C_4 = -\frac{\frac{1}{\alpha} + \langle T(x,y)\rangle - T_0}{\cosh\left(\sqrt{\frac{q_0\alpha}{\kappa}}a\right) + \frac{\kappa}{h}\sqrt{\frac{q_0\alpha}{\kappa}}\sinh\left(\sqrt{\frac{q_0\alpha}{\kappa}}a\right)} \tag{A36}$$

which is equivalent to equation 19 of the main body of the article. Therefore, the complete solution of the non-homogeneous ordinary differential equation is

$$\phi(x) = \frac{1 + \alpha\langle T(x,y)\rangle}{\alpha} - \frac{\frac{1}{\alpha} + \langle T(x,y)\rangle - T_0}{\cosh\left(\sqrt{\frac{q_0\alpha}{\kappa}}a\right) + \frac{\kappa}{h}\sqrt{\frac{q_0\alpha}{\kappa}}\sinh\left(\sqrt{\frac{q_0\alpha}{\kappa}}a\right)}\cosh\left(\sqrt{\frac{q_0\alpha}{\kappa}}x\right) \tag{A37}$$

On the other hand, the solution to the homogenous partial differential equation of $\varphi(x,y)$ can be obtained by using separation of variables $\varphi(x,y) = X(x)Y(y)$ and substituting in the equation A33. Doing so, one gets

$$\frac{\ddot{X}}{X} = -\frac{\ddot{Y}}{Y} + \frac{q_0\alpha}{\kappa} = -\lambda^2 \tag{A38}$$

where λ is a constant. Note that equation A38 is a similar eigenvalue problem to the one depicted in appendix II equation A10.

The solution to the ordinary differential equations for $X(x)$ (i.e. $\ddot{X} + \lambda^2 X = 0$) and $Y(y)$ (i.e. $\ddot{Y} - ((q_0\alpha)/\kappa + \lambda^2)Y = 0$) is straightforward and can be expressed as

$$X(x) = D_9\cos(\lambda x) + D_{10}\sin(\lambda x) \tag{A39}$$

The coefficients D_i are constants to be determined with the boundary conditions. Applying the first boundary condition in equations A34 at $x = 0$, the coefficient D_{10} vanishes in order to avoid trivialities. Using the second boundary condition of equation A34, one gets the transcendental equation

$$\lambda_n a \tan(\lambda_n a) = \frac{ha}{\kappa} = \text{Bi} \tag{A40}$$

By introducing $\Lambda_n = \lambda_n a$, equation A40 can be expressed as $\Lambda_n \tan(\Lambda_n) = \text{Bi}$.

On the other hand, the solution for $\ddot{Y} - ((q_0\alpha)/\kappa + \lambda^2)Y = 0$ is given by $Y(y) = D_{11}\cosh(C_{7,n}y/a) + D_{12}\sinh(C_{7,n}y/a)$, where $C_{7,n}$ is given in equation 22 of the main body of the article. By applying the third boundary condition in A34, the coefficient D_{12} is vanished. The fourth boundary condition at $y = b$ in equation A34 gives the condition

$$C_{7,n}C_{6,n}\frac{\kappa}{a}\cos\left(\Lambda_n\frac{x}{a}\right)\sinh\left(C_{7,n}\frac{b}{a}\right) + h\left[C_{6,n}\cos\left(\Lambda_n\frac{x}{a}\right)\cosh\left(C_{7,n}\frac{b}{a}\right)\right] = -h(\phi(x) - T_0) \tag{A41}$$

where $\phi(x)$ is already given in equation A37 and $C_{6,n}$ is the multiplication of D_9 times D_{11}. Finally, the coefficient $C_{6,n}$ is obtained by multiplying on both sides by $\cos\left(\Lambda_m\frac{x}{a}\right)$ and integrating on x over the width from $-a$ to a. Applying orthogonality, $m = n$ for having a solution, and $C_{6,n}$ would then result on the expression of equation 21 of the main body of the article.

Once $C_{6,n}$ is known, it can be inserted in the expression for $\varphi(x, y)$ and the solution for the temperature field $T(x, y)$ will then be

$$T(x,y) = \langle T\rangle + \sum_{n=1}^{\infty} C_{6,n}\cos\left(\Lambda_n\frac{x}{a}\right)\cosh\left(C_{7,n}\frac{y}{a}\right) + \frac{1}{\alpha} + C_4\cosh\left(C_5\frac{x}{a}\right) \tag{A42}$$

N.B. Similarly to what was already explained in appendix II, if equation A35 was equated to a positive eigenvalue λ^2 (instead of $-\lambda^2$) the solution will not be mathematically possible. This is because, in this case, $X(x) = D_9\cosh(\lambda x) + D_{10}\sinh(\lambda x)$, where D_{10} would become zero thanks to the first boundary condition of equation A31. The second boundary condition would lead to $\lambda a\tanh(\lambda a) = -\text{Bi}$, which means that λ has one imaginary solution. Finally, the square of an imaginary number results in a negative number, therefore the original statement of having a positive eigenvalue λ^2 instead of $-\lambda^2$ is not valid.

Appendix VI: Mesh convergence study of the "Bare SMC" and "SMC With Grips" geometries used during the numerical analysis of resistive heating.

A mesh convergence study is performed in both geometries used for the numerical analysis in Ansys in order to determine the minimum number of elements required to achieve an accurate prediction of resistive heating in the "Bare SMC" and "SMC With Grips" geometries. In order to save computational time and memory, one has taken advantage, whenever possible, of symmetry by just representing a quarter of the geometry and applying symmetry as a boundary condition.

Several simulations were run with increasing number of elements and the average temperature on the surface of the SMC was tracked. Figure A1 shows the average temperature on the surface for both the "Bare SMC" and the "SMC With Grips" with increasing number of elements. As it can be seen, the average temperature on the surface of the SMC starts converging to the same calculated value at a number of elements equal to 2500 and 18500 for the "Bare SMC" and "SMC With Grips" respectively. These are the two meshes used for the investigations presented in the main body of the article.

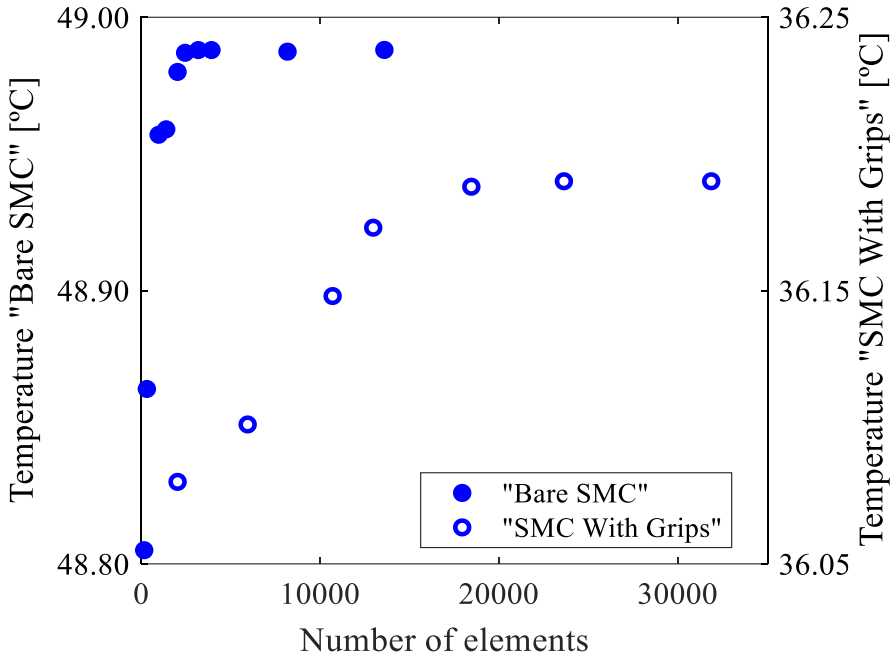

Figure A1: Mesh convergence study for the geometries "Bare SMC" and "SMC With Grips" used for the numerical analysis in Ansys of resistive heating of a SMC

Appendix VII: Properties of MWCNT Nanocyl 7000, data taken from the manufacturer

Table A1: Characteristics of the MWCNT Nanocyl 7000 used in the shape memory composites (data taken from the manufacturer's datasheet).

Parameter	Value
Average diameter [nm]	9.5
Average length [µm]	1.5
Carbon purity [%]	90
Transition metal oxide [%]	<1
Surface Area [$m^2 \cdot kg^{-1}$]	0.25-0.3
Volume resistivity [$\Omega \cdot m$]	1e-5